# PHOTONICS Research

# Optical trapping-enhanced probes designed by a deep learning approach

Miao Peng,[1,†] Guangzong Xiao,[2,3,†,*] Xinlin Chen,[2,3] Te Du,[4] Tengfang Kuang,[2,3] Xiang Han,[2,3] Wei Xiong,[2,3] Gangyi Zhu,[5] Junbo Yang,[4] Zhongqi Tan,[2,3] Kaiyong Yang,[2,3] and Hui Luo[2,3]

[1]*College of Sciences, Central South University of Forestry and Technology, Changsha 410004, China*
[2]*College of Advanced Interdisciplinary Studies, National University of Defense Technology, Changsha 410073, China*
[3]*Nanhu Laser Laboratory, National University of Defense Technology, Changsha 410021, China*
[4]*Center of Material Science, National University of Defense Technology, Changsha 410073, China*
[5]*College of Communication and Information Technology, Nanjing University of Posts and Telecommunications, Nanjing 210003, China*
[†]*These authors contributed equally to this work.*
*Corresponding author: xiaoguangzong@nudt.edu.cn*

**Realizing optical trapping enhancement is crucial in biomedicine, fundamental physics, and precision measurement. Taking the metamaterials with artificially engineered permittivity as photonic force probes in optical tweezers will offer unprecedented opportunities for optical trap enhancement. However, it usually involves multi-parameter optimization and requires lengthy calculations; thereby few studies remain despite decades of research on optical tweezers. Here, we introduce a deep learning (DL) model to attack this problem. The DL model can efficiently predict the maximum axial optical stiffness of $Si/Si_3N_4$ (SSN) multilayer metamaterial nanoparticles and reduce the design duration by about one order of magnitude. We experimentally demonstrate that the designed SSN nanoparticles show more than twofold and fivefold improvement in the lateral ($k_x$ and $k_y$) and the axial ($k_z$) optical trap stiffness on the high refractive index amorphous $TiO_2$ microsphere. Incorporating the DL model in optical manipulation systems will expedite the design and optimization processes, providing a means for developing various photonic force probes with specialized functional behaviors.      © 2024 Chinese Laser Press**

https://doi.org/10.1364/PRJ.517547

## 1. INTRODUCTION

Optical tweezers, which are exquisite displacement and force transducers, are widely applied in quantum optomechanics [1,2], biology [3,4], and nanotechnology [5,6]. Small dielectric particles are typically used as the photonic force probe and often act as handles for high-resolution measurements. However, the force range of these particles is usually around a few pN (with the laser power of tens to hundreds of milliwatts) [7], hindering the development of techniques and studies based on it. The optical force relies on the refractive index mismatch between the photonic force probes and the surrounding media. High-refractive-index particles, such as Si, rutile or anatase $TiO_2$, and $ZrO_2$, have sizeable refractive index mismatches [8–11]. However, as the mismatch increases, the instability scattering force increases more strongly than the gradient force.

Diverse solutions have developed to compensate for the adverse effect of scattering on trapping [12–14]. The simplest way is to modify the particle surface with an antireflection layer.

Titanium dioxide-coated titania particles can significantly enhance optical forces to 1 nN [15]. Nevertheless, the microsphere size suffers tight tolerance since a 10% change in the shell size would destabilize the trap [16]. In our previous work, we proposed the $ZrO_2@TiO_2$ core-shell nanoparticles to enhance the optical trapping in the nanoscale [9]. During the study, we found that numerous chemical synthesis experiments are needed to improve the accuracy of particle size. It usually requires rich experience and dedicated effort from experts in material engineering. This synthesis protocol is usually time-consuming and limited by the laboratory environment. Therefore, a probe design scheme with optical trap enhancement and precise size control is urgently needed to mitigate such a barrier.

Recent advances in nanofabrication technology have spurred many breakthroughs in optical metamaterials that can solve the above challenges [17–19]. Metamaterials are 3D artificial materials with tailored permittivity that are capable of large-volume production with high uniformity. The latest works

show they can act as light-driving objects to enhance optical torque, construct optical metavehicles, and even explore solar sails [20–22]. However, most of these are typically governed by hand-tuning the optical parameters. Manual tuning often takes hundreds or thousands of simulations before finding a practical design. Since each simulation is computationally expensive, this method becomes prohibitively slow as the probe size and complexity grow.

In contrast to manual tuning, the rapidly emerging deep learning (DL) algorithms can speed up the optimization cycle and introduce remarkable design flexibility. At present, DL algorithms have emerged as a revolutionary and robust methodology in nanophotonics and have been applied in diverse fields [23–27]. The critical algorithms of the DL model are artificial neural networks (NNs) [28,29], which take the input of the structural parameter and predict the electromagnetic response of the probe. These NNs replace the computationally expensive finite element simulations in the optimization loop, significantly reducing design time.

This work proposes a DL algorithm to predict the maximum axial optical stiffness of $Si/Si_3N_4$ multilayer metamaterial (SSN) nanoparticles with various geometry parameters. The SSN nanoparticles are fabricated according to the predicted value and characterized in an optical trap by measuring their power spectral density (PSD). The trapping properties of the SSN nanoparticles are superior to homogeneous high refractive index nanoparticles. This DL network can bypass the obstacles set by manual tuning, suggesting a new way to train NN for the optimal design of complex photonic force probes, which is the fundamental motivation of this study.

## 2. METHODS

In the Rayleigh regime [30], the gradient force is proportional to $\Delta n$ and $W^3$, and the scattering force is proportional to $\Delta n^2$ and $W^6$. $W$ is the width or diameter of the trapped particles, and $\Delta n = n_{eff} - n_m$, where $n_m$ and $n_{eff}$ are the refractive indices of the surrounding medium and particles. We select Si ($n_1 = 3.48$), the naturally occurring material with the highest refractive index, as the primary material to improve the gradient force. Then, $Si_3N_4$ ($n_2 = 1.98$) is selected as the matching material to decrease the scattering force according to the design of anti-reflection film [31]. That is, $n_2 = \sqrt{n_m n_1}$. Meanwhile, we use the cuboid instead of the commonly used sphere. This geometry decreases light scattering for a fixed volume of a particle by reducing the surface area encountered by the input laser beam [32]. Using the effective medium theory (EMT) [33], the high refractive index Si and $Si_3N_4$ are alternately superimposed to form multilayer metamaterial particles with high $n_{eff}$, thereby increasing $\Delta n$ to enhance the gradient force.

Figure 1(a) is the schematic diagram of the SSN nanoparticle composed of $Si_3N_4$ (blue) and Si (magenta) with its long axis aligned to the propagation direction (z-axis) of the trapping beam (light red). The trapping beam is linearly polarized along the x-axis. The cross-section of the SSN nanoparticle in the $x - y$ plane is a square with a width of $W$. The aspect ratio AR is the ratio of height $H$ to width $W$. The $\rho$ is the thickness ratio of the higher index material layer $d_1$ and the unit

layer-pair ($d_1 + d_2$). The value of $W$ ranges from 50 to 500 nm, AR ranges from 1 to 5, and $\rho$ ranges from 0.1 to 0.9. To ensure the structural symmetry of the particles, the thickness of the $Si_3N_4$ films on both sides is half of the normal thickness. The optics axis ($n_\perp$) of the SSN nanoparticle aligns with the y-axis, while the axes associated with the higher refractive index ($n_\parallel$) align with the x- and z-axes. The optical birefringence in the $x - y$ plane enables active rotary control around the z-axis (indicated by the blue curved arrow).

Figure 1(b) shows the relationship of the refractive index ($n_o$, $n_e$, $n_{eff}$), birefractive index ($n_r$), and $\rho$ of SSN nanoparticles. The refractive index along the ordinary axes ($n_o = n_\parallel = \sqrt{\varepsilon_\parallel}$) exceeds that along the extraordinary axis ($n_e = n_\perp = \sqrt{\varepsilon_\perp}$), indicating that the SSN nanoparticles are with a negative uniaxial birefringence ($n_e < n_o$). $\varepsilon_\parallel$ and $\varepsilon_\perp$ are the permittivity components parallel and perpendicular to the interfacial surfaces of the SSN nanoparticles, respectively [33]. The effective index [$n_{eff} = (n_e - n_o)/2$] varies from 1.98 (that of $Si_3N_4$) to 3.48 (that of Si), while the birefringence ($n_r = |n_e - n_o|$) can be tuned between zero and its maximum value ($n_r = 0.403$ when $\rho = 0.6$). The top-view and side-view of scanning electron microscope (SEM) images of the SSN nanoparticles with $\rho = 0.2$, $W = 450$ nm, and AR = 2 are shown in Figs. 1(c) and 1(d), respectively.

We use the finite element method (FEM) solver COMSOL Multiphysics 5.6 to design the SSN nanoparticle. The optical force is retrieved by integrating the Maxwell stress tensor (MST) on a virtual surface enclosing the nanoparticle [34]. We use the grid search algorithm to determine the optimal $\rho$ to reduce the number of optimized parameters. The $k_z$ for different $\rho$ values is plotted in Fig. 2. The black pixels mean that the SSN nanoparticles cannot be trapped in these parameters. Each parameter search range is $\rho = 0.1–0.9$, $W = 50–500$ nm, and AR = 1–5, with the pixel size of $\Delta\rho = 0.1$, $\Delta W = 10$ nm, $\Delta AR = 0.2$. The nanoparticles with $\rho = 0.2$, 0.4–0.9 are trappable over the entire range of $W$ and AR. Although the $k_z$ of the $\rho = 0.4–0.9$ nanoparticles can be maximized by selecting nanoparticle sizes in the bright yellow region at the bottom of the map, in practice their utilization in 3D trapping is difficult. Due to variations in nanoparticle sizes during manufacturing, some batches of particles will lie outside of the bright yellow region, leading to unstable trapping. Therefore, we selected nanoparticles with $\rho = 0.2$ in the DL optimization process. In particular, the nanoparticles with $\rho = 0.1$ and 0.3 include continuous non-trappable regions displayed as black pixels in Figs. 2(a) and 2(c). For the sake of "intelligence," we select $\rho = 0.3$ to verify the accuracy and applicability of the DL network. The maximum value can still be found accurately in the discontinuous parameter space.

We perform the DL network based on the NN and particle swarm optimization (PSO) hybrid optimization (NN-PSO) algorithm to find the optimal $W$ and AR. First, $W$ and AR are divided into several grids. As shown in Fig. 3, a random grid (e.g., $W = 250–300$ nm, AR = 4 − 5, $\Delta W = 1$ nm, $\Delta AR = 0.1$, $M = 561$) is selected as the training set $D_1(W_i, AR_i, k_{zi})$, $i = 1, 2, …, M$, serving as the input layer of NN. Subsequently, we establish a mapping between $W$,
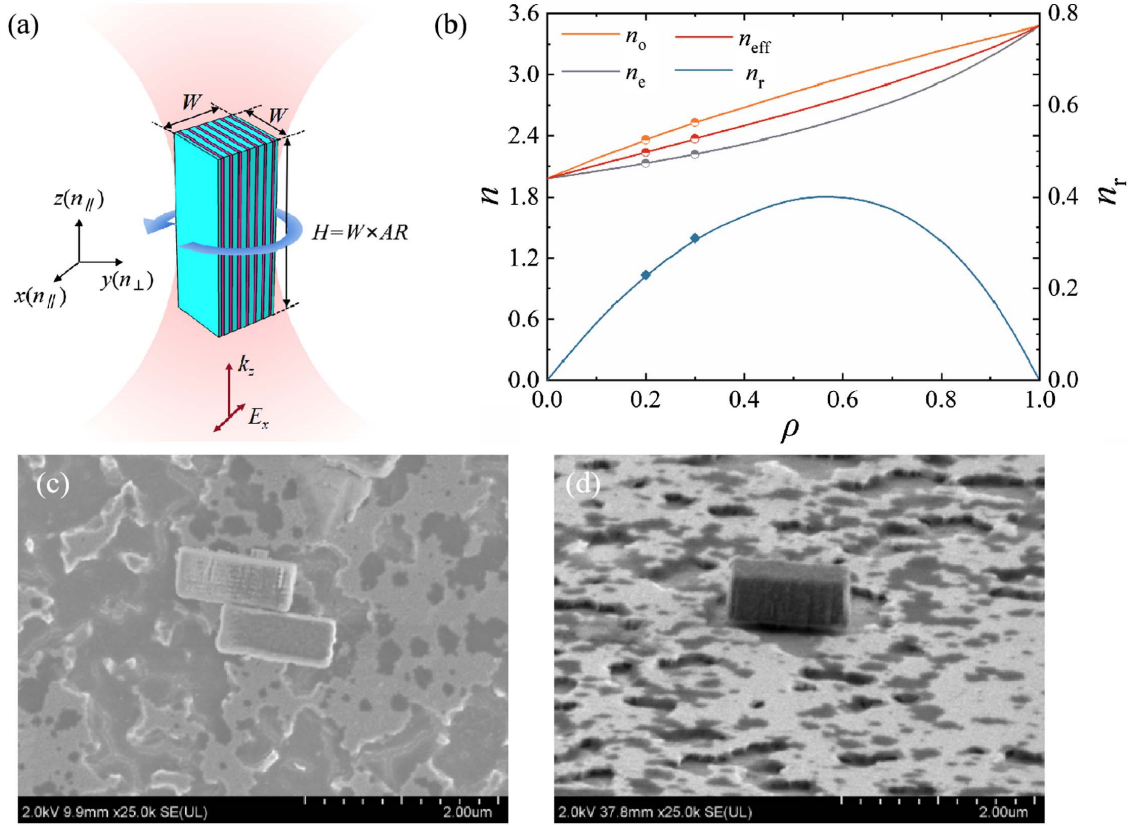
**Fig. 1.** (a) The schematic of the trapped SSN nanoparticle, which is made of Si (magenta) and $Si_3N_4$ (blue), with its long axis aligned to the optical axis ($z$-axis) of the trapping beam (red). The cross section in the $x$ – $y$ plane is a square of width $W$, and the aspect ratio AR is the ratio of height $H$ to width $W$. (b) The effective refractive indices and birefringence of the SSN nanoparticles as a function of $\rho$. (c) Top-view and (d) side-view of SEM images of SSN nanoparticles with $\rho = 0.2$, $W = 450$ nm, and AR = 2.

AR, and $k_z$ to obtain the NN model. Then, we randomly select $W_i'$ and $AR_i'$ in $D_1$ and plug them into the NN model to quickly predict the corresponding $k_{zi}'$. These $k_{zi}'$ are regarded as the particles of PSO and grouped up as the initial population. Each $k_{zi}'$ has velocity $v_i$ and position $p_i$ $(W_i', AR_i')$. The $v_i$ determines how fast the $k_{zi}'$ moves, and the $p_i$ determines the direction in which the $k_{zi}'$ moves. We calculate the fitness $\Delta k_{zi}$ of each $k_{zi}'$. The $\Delta k_{zi}$ represents the difference between the current $k_{zi}''$ and the previous $k_{zi}'$ [35],

$$\Delta k_{zi} = \sum_{W_i'}\sum_{AR_i'} |k_{zi}''(p_i(W_i', AR_i')) - k_{zi}'(p_i(W_i', AR_i'))|. \tag{1}$$

Next, $\Delta k_{zi}$ is compared to find the optimal solution of the $k_{zi}'$, which is also called the individual extremum $P_i$. We share the $P_i$ with the population and find the global optimal solution $G_j$, where $j$ represents the training set number. If the requirements are satisfied, the iteration is ended. Otherwise, the $v_i$ and $p_i$ of each $k_{zi}'$ are updated. The algorithm enters the next iteration until the results converge to the optimal point. The $v_i$ and $p_i$ are as follows:

$$v_i = w \times v_i + c_1 \times rand(0, 1) \times (P_i - p_i(W_i, AR_i)) + c_2$$
$$\times rand(0, 1) \times (G_j - p_i(W_i, AR_i)), \tag{2}$$

$$p_{i+1}(W_{i+1}, AR_{i+1}) = p_i(W_i, AR_i) + v_i, \tag{3}$$

where $w$ is the inertia factor set to 0.5, $c_1$ and $c_2$ are the learning factors, with values of 0.5, and rand (0, 1) is a random number in the interval (0, 1).

## 3. RESULTS AND DISCUSSION

### A. Estimation of the NN-PSO Model

We evaluate the performance of the NN-PSO model in predicting the optimal $k_z$ of SSN nanoparticles with $\rho = 0.2$ and 0.3, with the results shown in Figs. 4(a) and 4(b). Figure 4(a) shows the optimization process for the SSN nanoparticles at $\rho = 0.2$. White arrows indicate that we need five steps to find the globally optimal solution (blue dot). The circled numbers (① to ⑥) indicate that only six grids need to be computed to find the optimal $k_z$. The optimal $k_z$ is 1.7 pN $\mu m^{-1}$ mW$^{-1}$, and the optimal parameters are $W = 450$ nm, $H = 1125$ nm, and AR = 2.5.

Figure 4(b) shows the optimization process for the SSN nanoparticles at $\rho = 0.3$. Black arrows indicate that we only need two steps to find the optimal $k_z$. We randomly select grid ① as the initial training set. Since the larger $k_z$ in grid ② is near the right edge, grid ② is chosen as the next training set. The larger $k_z$ in grid ② is concentrated at the bottom of the lower boundary, indicating the maximum value below grid ②.
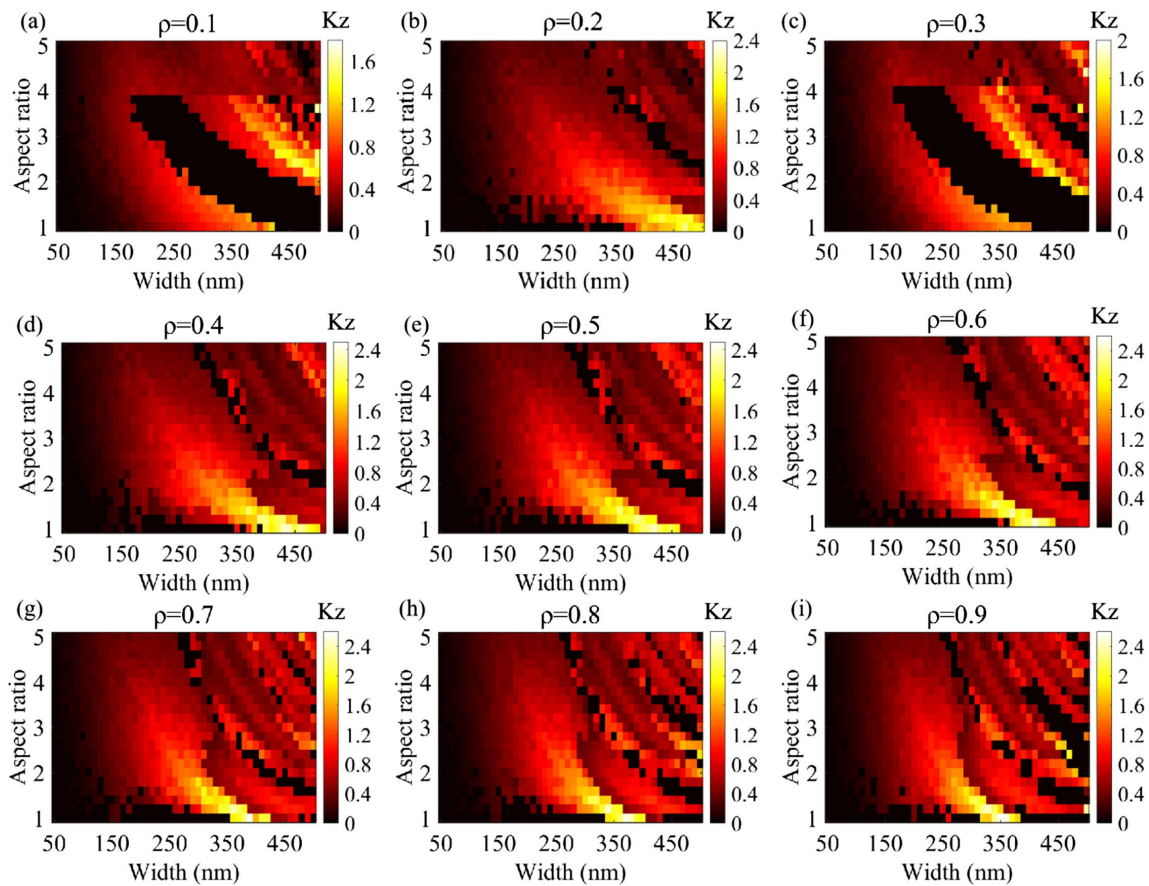
**Fig. 2.** The relationship between the axial stiffness $k_z$ of SSN nanoparticles and the width $W$, aspect ratio $AR$ under different $\rho$ values. (a) $\rho = 0.1$, (b) $\rho = 0.2$, (c) $\rho = 0.3$, (d) $\rho = 0.4$, (e) $\rho = 0.5$, (f) $\rho = 0.6$, (g) $\rho = 0.7$, (h) $\rho = 0.8$, (i) $\rho = 0.9$. The black pixels in the maps indicate the nanoparticle sizes that cannot be trapped in 3D due to excessive scattering forces.

We calculate grid ③ and grid ④, respectively. The results show that the global optimal solution is in grid ③ (blue dot). The predicted $k_z$ is 1.6 pN μm$^{-1}$ mW$^{-1}$, and the optimal parameters are $W = 383$ nm, $H = 1110.7$ nm, AR = 2.9.

**B. Trapping Properties of the SSN Nanoparticles**
Guided by the results above, we fabricated and characterized the SSN nanoparticles with $\rho = 0.2$, whose sizes are $W = 450$ nm, $H = 1125$ nm, and AR = 2.5, and the $n_{\text{eff}}$ is 2.24. The fabrication process is shown in Appendix A. The SEM images of these SSN nanoparticles are shown in Figs. 1(c) and 1(d). To measure the trapping properties of the SSN nanoparticles, we then optically trapped them in a standard optical tweezers system [36,37]. The laser is a linearly polarized fundamental mode Gaussian beam along the $x$ direction with power and wavelength as 100 mW and 980 nm, respectively. An oil-immersed objective with a numerical aperture (NA) of 1.4 is used to ensure the stable trap of nanoparticles. We developed a homemade sample chamber to match the working distance of the oil-immersed objective. (The details are supplemented in Appendix A.) We detected the $x$- and $y$-positions of the trapped nanoparticle by quadrant detectors (QPDs) and measured the axial ($z$-) displacement by a differential detection unit. The optical stiffness is calculated using the power spectrum analysis method [38]. For comparison,

we trapped a high refractive index (1.75) amorphous TiO$_2$ microsphere with a radius of 600 nm. (The trapping efficiency is highest at this radius; see Appendix B.)

We confirm the tight 3D-trapping of the two types of particles by measuring the PSD, as shown in Fig. 5. We use the formula $k = 2\pi\eta f_c$ to calculate the optical trap stiffness, where $\eta$ is the viscous drag coefficient [34]. The corner frequency $f_c$ is obtained by fitting the power spectrum with the Lorenz profile. The 3D $f_c$ and optical trap stiffness corresponding to the SSN and amorphous TiO$_2$ particles are listed in Table 1. Overall, the lateral ($k_x$ and $k_y$) and the axial ($k_z$) optical trap stiffness of the SSN nanoparticles is twofold and fivefold higher than that of the amorphous TiO$_2$ microspheres. This difference results from their higher refractive index contrast (22%) and ensures a higher optical gradient force for the SSN nanoparticles. In addition, the rod-shaped SSN nanoparticles decrease the scattering force by reducing the surface area encountered by the incident light.

The SSN nanoparticles are negative uniaxial birefringent crystals, and the birefringence-originated torque constrains only one rotational degree of freedom (RDOF). The drawback is that unconstrained RDOF may introduce unexpected angular fluctuations into the displacement signal. The geometric anisotropy provided by a rod shape can compensate for this
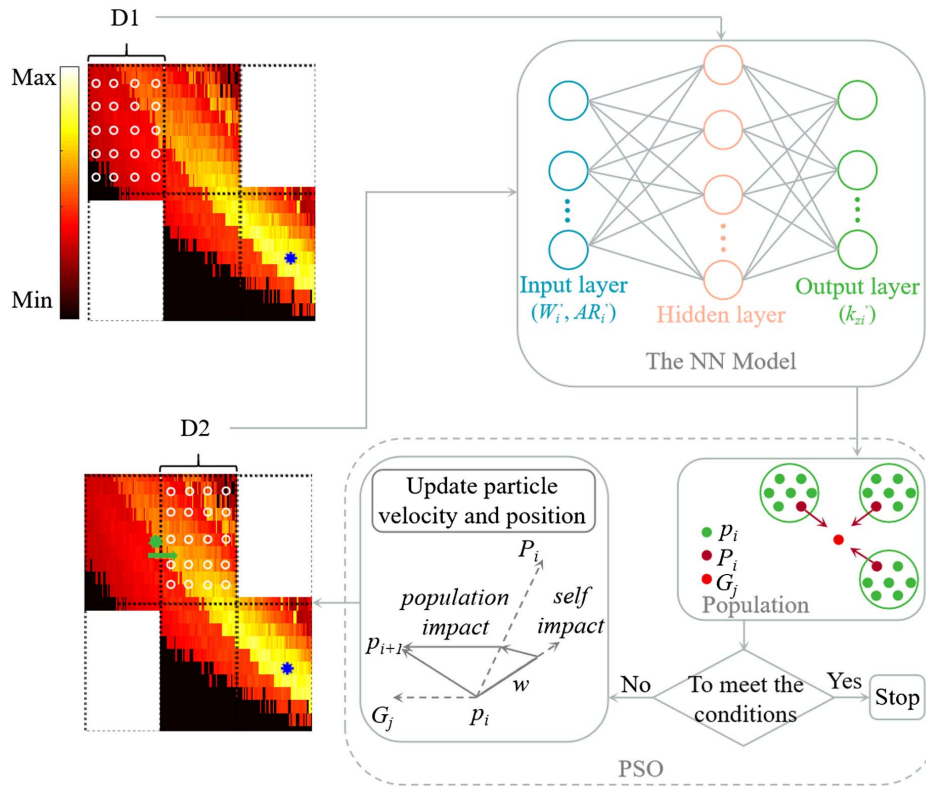
**Fig. 3.** Architecture of the DL network based on the NN-PSO algorithm, where the input is the size parameters and the output is the $k_z$.
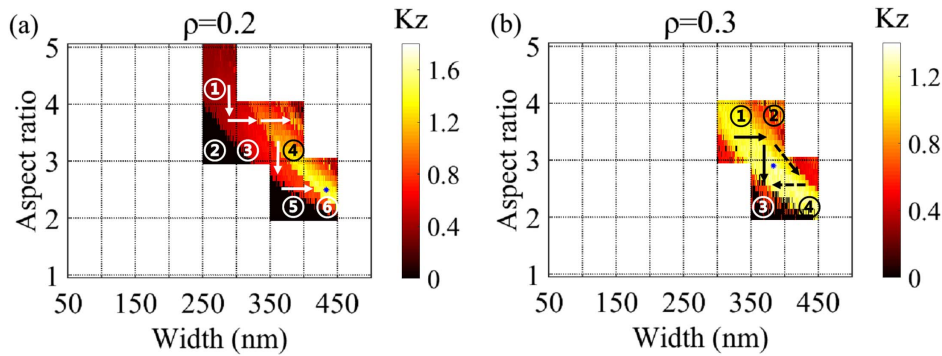


**Fig. 4.** The $k_z$ optimization process for $\rho = 0.2$ (a) and 0.3 (b), respectively. The arrow indicates the route to find the optimal solution. The circle numbers indicate the number of the grid to be calculated in that route, and the blue dot indicates the optimal solution.
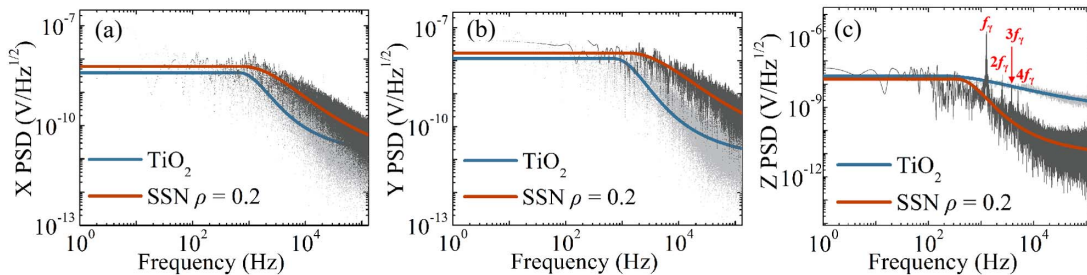


**Fig. 5.** The $x$- (a), $y$- (b), and $z$- (c) axis power spectral density curves for two types of particles (SSN and $TiO_2$) measured in water.

**Table 1.    Trapping Parameters of Two Kinds of Particles in Water**

| Types | Corner Frequency $f_c$ (Hz) | | | Optical Trap Stiffness $k$ (pN μm⁻¹ mW⁻¹) | | |
| --- | --- | --- | --- | --- | --- | --- |
| | $f_{cx}$ | $f_{cy}$ | $f_{cz}$ | $k_x$ | $k_y$ | $k_z$ |
| SSN | 1179 | 1304 | 850 | 0.75 | 0.83 | 0.54 |
| TiO₂ | 675 | 729 | 174 | 0.43 | 0.46 | 0.11 |

drawback and sufficiently constrain the three RDOFs (Fig. 10 of Appendix C). Further, the influence of spin on $k_z$ is analyzed (Fig. 11 of Appendix C). Figure 5(c) shows an optical beating at $2f_\gamma$ when the nanoparticle rotates at a spin frequency of $f_\gamma (= 1276 \text{ Hz})$. We remark that higher harmonics of the fundamental rotation frequency of $f_\gamma$ are also observed in the PSD signal. The Cr fragment or impurity remaining on the SSN nanoparticle surface leads to the uneven distribution of the scattered and transmitted light, resulting in variations in the photodiode signal.

## 4. CONCLUSION

In this study, we have introduced the deep learning algorithm in the design of optical trapping-enhanced probes. The deep learning algorithm provides a time-saving way to replace the computationally expensive FEM simulations in the optimization loop, reducing the design duration by about one order of magnitude. Notably, we have achieved at least a twofold and fivefold improvement in the lateral ($k_x$ and $k_y$) and the axial ($k_z$) optical trap stiffness, respectively, compared to the amorphous TiO₂ microsphere in water.

We envision several compelling extensions of this work. For example, one can precisely control the particle size using advanced thin-film deposition and lithography techniques. This strategy can bypass the limitation set by the size tolerance originating from the chemical synthesis scheme [16], suggesting a new way to fabricate probes on the nanoscale. On

the other hand, the biochemical inertness, insolubility of Si/Si₃N₄ nanoparticles, together with their optical trap enhancement characteristics, will facilitate their application in *in vivo* manipulation of cells [39] or in optofluidics [40,41]. The rotation effect of multilayer metamaterial makes it possible to use them as micro-motors to construct hydrodynamic optical tweezers for biological targeted therapy [42]. Significantly, benefiting from the deep learning algorithm, compared with the manual tuning, this work opens the door to a highly efficient design of photonic force probes, spanning from the nanoscale to the microscale. Together, optical trap enhancement with deep learning algorithms makes multilayer metamaterial nanoparticles up-and-coming candidates for optomechanical systems in science and engineering.

## APPENDIX A: FABRICATION PROCESS OF SSN NANOPARTICLES

We use a top-down fabrication process to fabricate the SSN nanoparticles, as shown in the Fig. 6. (1) A four-inch Si wafer is cleaned. (2) A 100-nm-thick sacrificial chromium (Cr) layer is deposited on the Si wafer by electron-beam evaporation. (3) The SSN multilayer is deposited using plasma-assisted reactive magnetron sputtering. (4) A positive-tone resist layer with a thickness of 250 nm is spin-coated. (5) The resist layer is patterned by electron-beam lithography. (6) The patterned resist layer is developed with ultrasonication, sequentially with the 50-nm-thick Cr etch mask layer deposited by
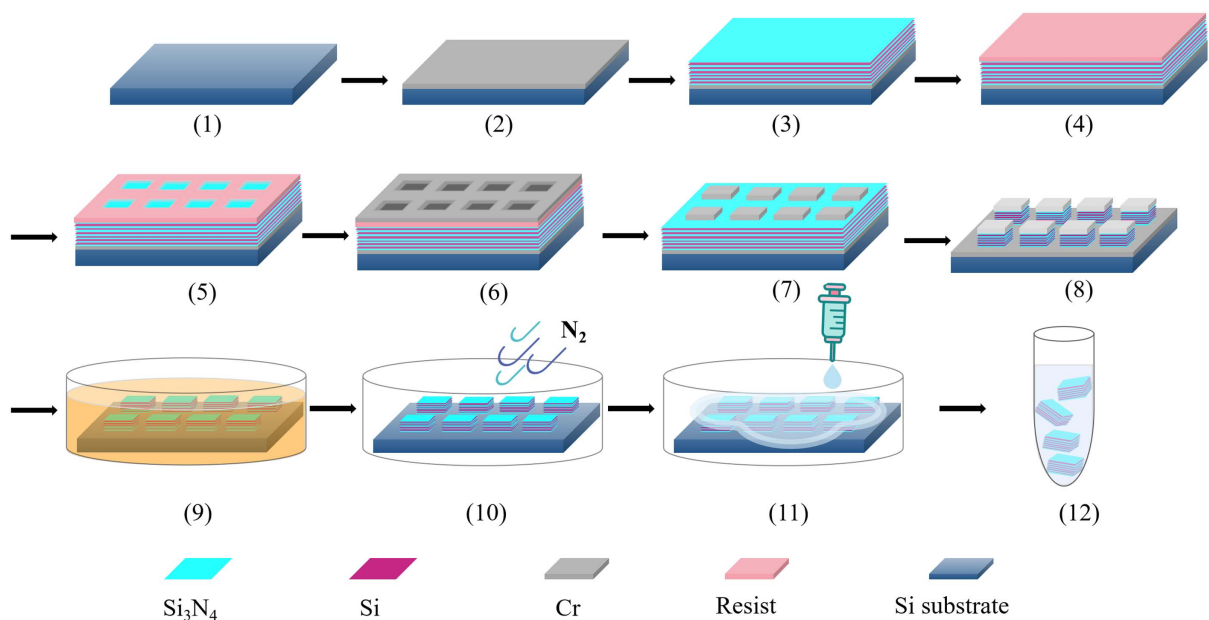


**Fig. 6.**    The fabrication process of SSN nanoparticles. (The legend is the color coding for different materials.)

Ar-plasma sputtering. (7) In the lift-off process, the top Cr layer is initially removed by the adhesive tape and then the remaining resist layer is removed by dipping the sample in resist stripper solution. (8) A reactive ion etcher is used vertically to etch the multilayer. (9) The samples are manually cleaved into 1 cm × 1 cm chips and then immersed in a petri dish containing Cr etchant solution (orange color, with 10%–20% ammonium cerium nitrate and 5%–15% nitric acid) for 7 min, where the top Cr mask and the bottom sacrificial Cr layer of the SSN nanoparticles are dissolved altogether. (10) Then, take the sample with tweezers and gently place it flat in dry glassware and dry treatment with a nitrogen atmosphere. (11) A small drop of deionized (DI) water is dropped on the surface of the samples, and most of the multilayer units on the surface are released in this water droplet due to the surface tension of the water. (12) Take the sample with plastic tweezers very slowly from the glassware, where the water droplet is attached to the surface. The taken-out sample and the water droplet on its surface are transferred into a 1.5 mL centrifuge tube, followed by 30 s of ultrasound processing. We remove the remaining Si substrate and leave only the SSN nanoparticles in the DI water.

We determined the nanoparticle sizes by taking scanning electron microscopy (SEM) and atomic force microscopy (AFM) images after step (8). The top-view SEM images of the samples are shown in Figs. 7(a) and 7(b). The side-view SEM image of the samples is shown in Fig. 7(c). The SSN nanoparticles are patterned in a square array with a gap length of 20 μm, and the single unit cell has a width and length of 450 nm and 1125 nm, respectively. Figure 7(d) shows the height of the unit cell as measured by AFM. The total height of the unit cell is 600 nm, where the height of the Cr sacrificial layer and the SSN nanoparticles is 150 nm and 450 nm, respectively.

In addition, we set the time gradient during the wet etching process to determine the exact dissolution time of the Cr sacrificial layer, as shown in Fig. 8. The sample is first placed in the Cr etchant solution shown in step (9) for 47 s and then dried in the nitrogen atmosphere shown in step (10). Moreover, we take the SEM to observe the etching effect, as shown in Fig. 8(a). We see that the etching is insufficient and repeat steps (9) and (10) at a new time gradient. Figure 8(c) shows that the top Cr mask is wholly etched at 120 s. Figure 8(d) shows that the bottom sacrificial Cr layer is completely dissolved at 7 min, and the substrate surface has traces of SSN nanoparticle stripping left. Figure 8(e) shows that SSN nanoparticles can move freely on the surface, indicating successful etching. The particles are subsequently collected using the scheme shown in steps (11) and (12). Figure 8(f) is the schematic of step (11). The final concentration of the collected solution is about $2 \times 10^4$ particles per μL.

We developed the homemade sample chamber to trap the SSN nanoparticles. First, a standard slide is affixed with a "doughnut" shaped 3M tape with a thickness of 100 μm. The particle dispersion is then drawn with a syringe and dripped
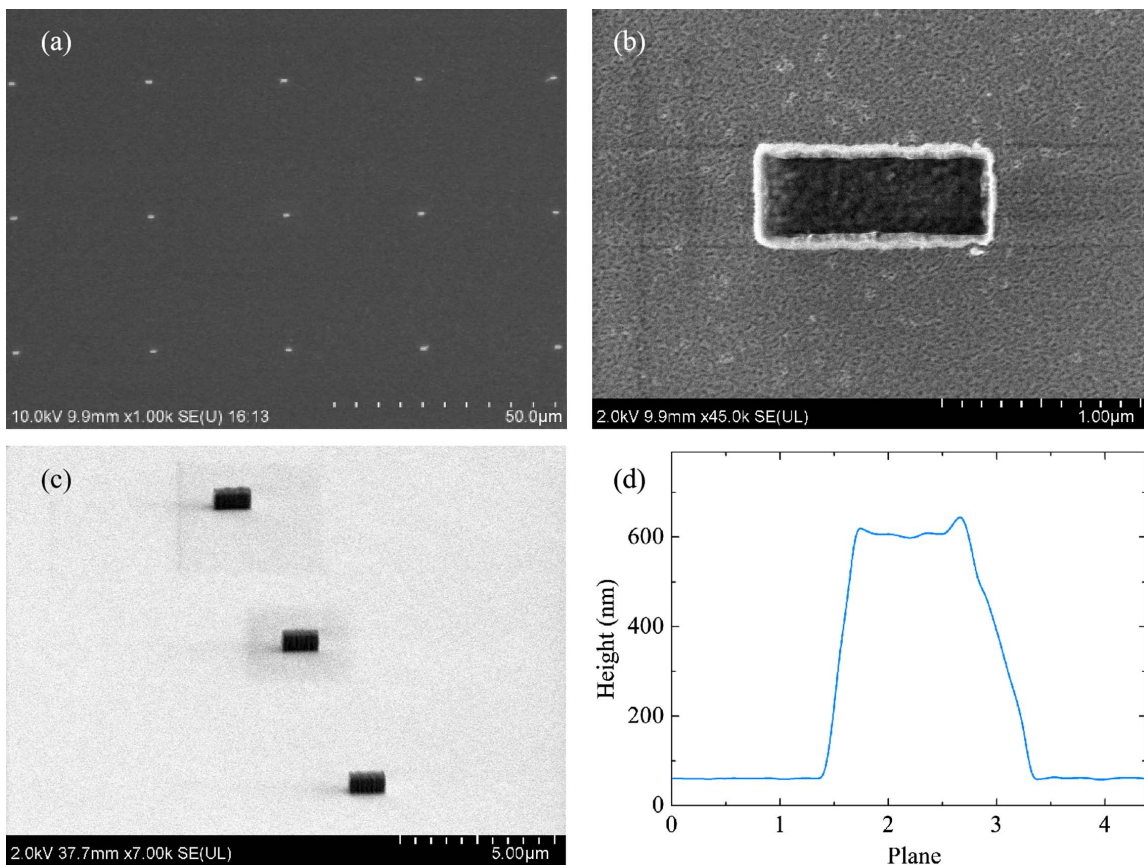


**Fig. 7.** Characterization of SSN nanoparticles. (a) and (b) SEM images of the sample shown In step (8). (d) Height of the unit cell as measured by AFM.
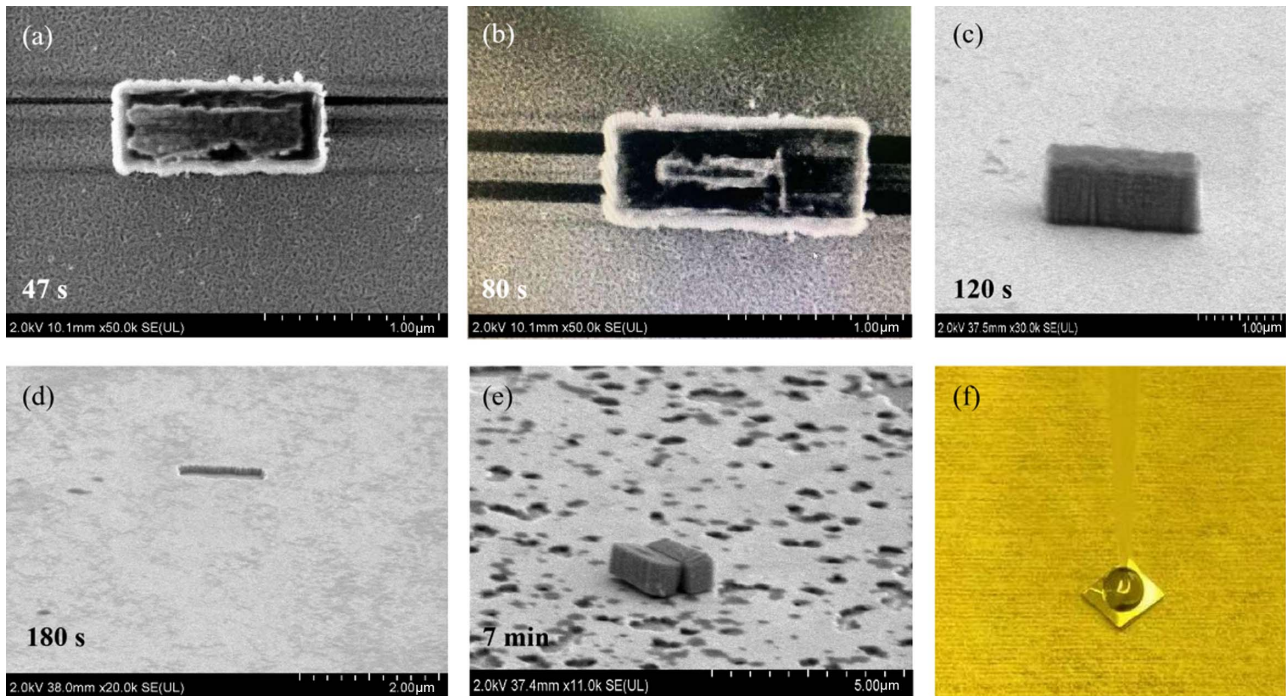
**Fig. 8.** To determine the exact dissolution time of the Cr sacrificial layer. (a) 47 s, (b) 80 s, (c) 120 s, (d) 180 s, (e) 7 min. (f) A small drop of DI water is dropped on the surface of the samples.

inside the "doughnut" ring. Finally, a custom cover glass with a thickness of 500 μm is covered, and the channel round is sealed with vacuum grease to prevent the sample from drying out. The chamber is filled with the SSN nanoparticle solution without any air bubbles.

## APPENDIX B: TRAPPING EFFICIENCY OF THE AMORPHOUS TiO$_2$ MICROSPHERE

We simulated the trapping efficiency as a function of the radius of the high refractive index (1.75) amorphous TiO$_2$ microsphere, as shown in Fig. 9. The blue and red curves are the axial ($Q_z$) and lateral ($Q_x$) trapping efficiency, respectively. We can see that the $Q_z$ and $Q_x$ reach the maximum value
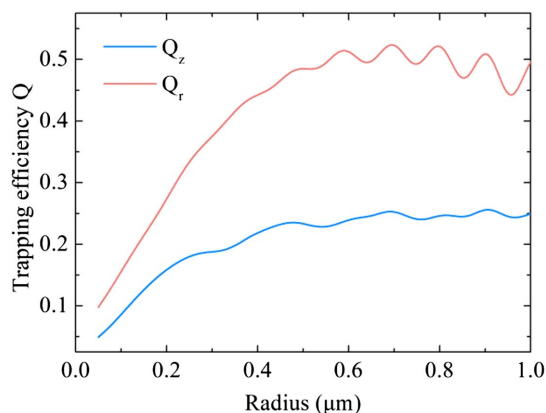


**Fig. 9.** The trapping efficiency as a function of the radius of the amorphous TiO$_2$ microsphere. The blue and red curves are the axial ($Q_z$) and lateral ($Q_x$) trapping efficiency, respectively.

at about 600 nm radius, and both tend to be stable with the increase of radius. Therefore, we chose the 600 nm radius amorphous TiO$_2$ microspheres as the comparison sample.

## APPENDIX C: ANGULAR TRAPPING BEHAVIOR OF SSN NANOPARTICLES

Figure 10 shows that the geometry and optical anisotropy of the SSN nanoparticles simultaneously limit all three rotational degrees of freedom (RDOFs). To analyze the influence of shape on torque, we compare the torques of cylindrical (blue curve) and rectangular (red curve) SSN nanoparticles, respectively. Figures 10(a) and 10(d) show the alignment torque $\tau_x$ [43], attributed to the high AR. After the high AR nanoparticles tilt at angles $\alpha$ ($x$ direction) relative to the optical axis ($z$-axis), the uneven surface stress distribution generates the torque $\tau_x$, which ensures the nanoparticle's long side is always parallel to the $z$-axis. Figures 10(b) and 10(e) show that the alignment torque $\tau_y$ is doubly confined by geometrical and optical anisotropy. $\beta$ is the angular displacement when the nanoparticle is tilted to $y$ direction relative to the optical axis. The geometrically dependent torque exceeds the torque due to the birefringence, which can align the negative uniaxial nanoparticles and ensure their optic axis ($n_\perp$) is parallel to the electric field. Therefore, the alignment torque always keeps the long side of the nanoparticles parallel to the optical axis, no matter how they fall into the trap.

Figures 10(c) and 10(f) show the spin torque $\tau_z$ [44], which is generated by the optical anisotropy on the $x$ – $y$ plane and the rotation in the linear polarization of the trapping beam. $\gamma$ is the rotation angle. Remarkably, the $\tau_z$ of the rectangular and cylindrical SSN nanoparticles is similar. Because the optical axis ($n_\perp$)
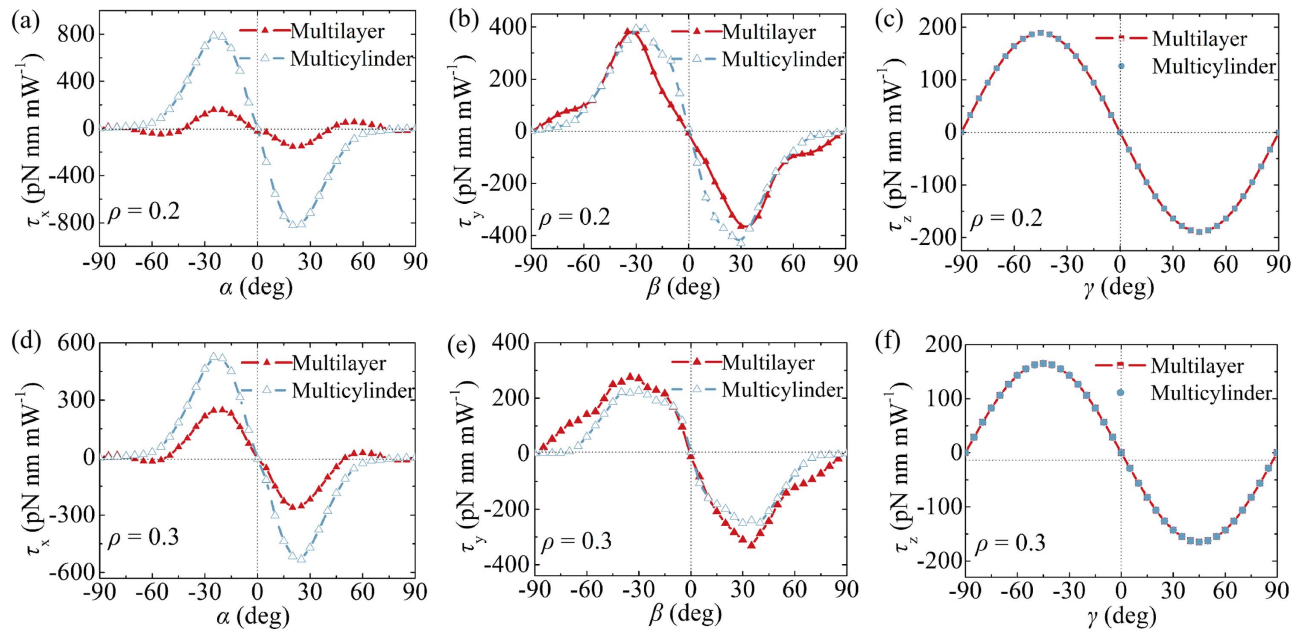
**Fig. 10.** The relationship between torques and the angular displacement for two shapes of SSN nanoparticles. $\rho = 0.2$, $\tau_x$ (a), $\tau_y$ (b), $\tau_z$ (c); $\rho = 0.3$, $\tau_x$ (d), $\tau_y$ (e), and $\tau_z$ (f). The blue and red curves represent cylindrical and rectangular SSN nanoparticles, respectively.

of the rectangular nanoparticles is perpendicular to its long side during the spin, the cylindrical nanoparticles are perpendicular to the tangential direction of the cylindrical side surface, essentially the same as the rectangular one. Since the rectangular SSN nanoparticles are easily fabricated by thin-film deposition techniques, such as hot evaporation [45], ion beam sputtering [46], and atomic layer deposition [47], we select rectangular shapes for processing. The maximum spin torque $\tau_z$ of the rectangular SSN nanoparticles at $\rho = 0.2$ is 189 pN nm mW$^{-1}$. Together with the rotational drag coefficient $\Gamma$, the maximum spin speed $f_z = \tau_z/(2\pi\Gamma)$ can be calculated. We build the Navier–Stokes equations [48] in the computational fluid dynamics module of COMSOL to extract $\Gamma$. The surrounding medium water is set to flow rotationally. The dynamic viscosity of water is 0.933 mPa s at 25°C. $\Gamma$ is 1.5 pN nm s. Thereby, $f_z$ is 2005 Hz.
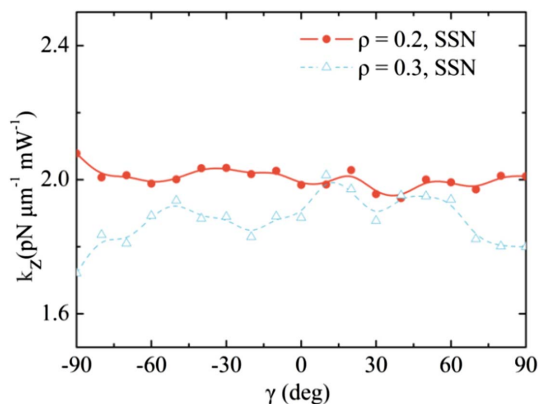
Figure 11 simulates the $k_z$ of trapped SSN nanoparticles at different rotation angles $\gamma$. The total fluctuation values [34] for $\rho = 0.2$ (red) and 0.3 (blue) are only 4% and 6.91%, respectively, indicating that the influence of spin on $k_z$ can be ignored.

**Disclosures.** The authors declare no competing financial interests.

**Data Availability.** Data underlying the results presented in this paper are not publicly available at this time but may be obtained from the authors upon reasonable request.



**Fig. 11.** Relationship between rotation angle $\gamma$ and $k_z$ when $\rho$ is 0.2 and 0.3, respectively.

## REFERENCES

1. T. Kuang, R. Huang, W. Xiong, *et al.*, "Nonlinear multi-frequency phonon lasers with active levitated optomechanics," Nat. Phys. **19**, 414–419 (2023).
2. T. Li, S. Kheifets, and M. G. Raizen. "Millikelvin cooling of an optically trapped microsphere in vacuum," Nat. Phys. **7**, 527–530 (2011).
3. X. Shan, F. Wang, D. Wang, *et al.*, "Optical tweezers beyond refractive index mismatch using highly doped upconversion nanoparticles," Nat. Nanotechnol. **16**, 531–537 (2021).

4. M. Zhong, X. Wei, J. Zhou, *et al.*, "Trapping red blood cells in living animals using optical tweezers," Nat. Commun. **4**, 1768 (2013).

5. P. J. Pauzauskie, A. Radenovic, E. Trepagnier, *et al.*, "Optical trapping and integration of semiconductor nanowire assemblies in water," Nat. Mater. **5**, 97–101 (2006).

6. O. M. Maragò, P. H. Jones, P. G. Gucciardi, *et al.*, "Optical trapping and manipulation of nanostructures," Nat. Nanotechnol. **8**, 807–819 (2013).

7. F. Hajizadeh and S. S. Reihani, "Optimized optical trapping of gold nanoparticles," Opt. Express **18**, 551–559 (2010).

8. S. Ha, Y. Tang, M. M. van Oene, *et al.*, "Single-crystal rutile $TiO_2$ nanocylinders are highly effective transducers of optical force and torque," ACS Photon. **6**, 1255–1265 (2019).

9. M. Peng, H. Luo, W. Xiong, *et al.*, "Enhanced optical trapping of $ZrO_2$@$TiO_2$ photonic force probe with broadened solvent compatibility," Opt. Express **30**, 46060–46069 (2022).

10. C. Min, Z. Shen, J. Shen, *et al.*, "Focused plasmonic trapping of metallic particles," Nat. Commun. **4**, 2891 (2013).

11. M. N. Polyanskiy, "Refractiveindex.info database of optical constants," Sci. Data **11**, 94 (2024).

12. V. Bormuth, A. Jannasch, M. Ander, *et al.*, "Optical trapping of coated microspheres," Opt. Express **16**, 13831–13844 (2008).

13. A. van der Horst, P. D. J. van Oostrum, A. Moroz, *et al.*, "High trapping forces for high-refractive index particles trapped in dynamic arrays of counterpropagating optical tweezers," Appl. Opt. **47**, 3196–3202 (2008).

14. M. L. Juan, R. Gordon, Y. Pang, *et al.*, "Self-induced back-action optical trapping of dielectric nanoparticles," Nat. Phys. **5**, 915–919 (2009).

15. A. Jannasch, A. F. Demirörs, P. D. OostrumVan, *et al.*, "Nanonewton optical force trap employing anti-reflection coated, high-refractive-index titania microspheres," Nat. Photonics **6**, 469–473 (2012).

16. V. Ferro, A. Sonnberger, M. K. Abdosamadi, *et al.*, "Improved antireflection coated microspheres for biological applications of optical tweezers," Proc. SPIE **9922**, 99222T (2016).

17. S. M. Wang, P. C. Wu, V. C. Su, *et al.*, "A broadband achromatic metalens in the visible," Nat. Nanotechnol. **13**, 227–232 (2018).

18. T. Li, X. Xu, B. Fu, *et al.*, "Integrating the optical tweezers and spanner onto an individual single-layer metasurface," Photon. Res. **9**, 1062–1068 (2021).

19. G. Qu, W. Yang, Q. Song, *et al.*, "Reprogrammable meta-hologram for optical encryption," Nat. Commun. **11**, 5484 (2020).

20. Y. Tang, S. Ha, T. Begou, *et al.*, "Versatile multilayer metamaterial nanoparticles with tailored optical constants for force and torque transduction," ACS Nano **14**, 14895–14906 (2020).

21. D. Andrén, D. G. Baranov, S. Jones, *et al.*, "Microscopic metavehicles powered and steered by embedded optical metasurfaces," Nat. Nanotechnol. **16**, 970–974 (2021).

22. O. Ilic and A. A. Harry, "Self-stabilizing photonic levitation and propulsion of nanostructured macroscopic objects," Nat. Photonics **13**, 289–295 (2019).

23. Y. Park and M. Kellis, "Deep learning for regulatory genomics," Nat. Biotechnol. **33**, 825–826 (2015).

24. S. Webb, "Deep learning for biology," Nature **554**, 555–557 (2018).

25. P. Baldi, P. Sadowski, and D. Whiteson, "Searching for exotic particles in high-energy physics with deep learning," Nat. Commun. **5**, 4308 (2014).

26. G. Carleo and M. Troyer, "Solving the quantum many-body problem with artificial neural networks," Science **355**, 602–606 (2017).

27. W. Ma, F. Cheng, and Y. Liu, "Deep-learning-enabled on-demand design of chiral metamaterials," ACS Nano **12**, 6326–6334 (2018).

28. Y. Shen, N. C. Harris, S. Skirlo, *et al.*, "Deep learning with coherent nanophotonic circuits," Nat. Photonics **11**, 441–446 (2017).

29. M. Hermans, M. Burm, T. Van Vaerenbergh, *et al.*, "Trainable hardware for dynamical computing using error backpropagation through physical media," Nat. Commun. **6**, 6729 (2015).

30. K. Svoboda and S. M. Block, "Biological applications of optical forces," Annu. Rev. Biophys. Biomol. Struct. **23**, 247–285 (1994).

31. S. Walheim, E. Schaffer, J. Mlynek, *et al.*, "Nanophase-separated polymer films as high-performance antireflection coatings," Science **283**, 520–522 (1999).

32. A. La Porta and M. D. Wang, "Optical torque wrench: angular trapping, rotation, and torque detection of quartz microparticles," Phys. Rev. Lett. **92**, 190801 (2004).

33. W. Cai and M. Vladimir, *Optical Metamaterials* (Springer, 2010).

34. M. Peng, H. Luo, Z. Zhang, *et al.*, "Optical pulling using chiral metalens as a photonic probe," Nanomaterials **11**, 3376 (2021).

35. Y. Wang, M. Peng, W. Cheng, *et al.*, "Manipulation force analysis of nanoparticles with ultra-high numerical aperture metalens," Opt. Express **30**, 28479–28491 (2022).

36. X. Chen, G. Xiao, W. Xiong, *et al.*, "Rotation of an optically trapped vaterite microsphere measured using rotational Doppler effect," Opt. Eng. **57**, 036103 (2018).

37. M. Pei, S. Jin, X. Chen, *et al.*, "Direct measurement of the van der Waals force between a pair of microspheres based on photonic force microscopy," Opt. Eng. **60**, 084101 (2021).

38. K. Berg-Sorensen and H. Flyvbjerg, "Power spectrum analysis for optical tweezers," Rev. Sci. Instrum. **75**, 594–612 (2004).

39. I. A. Favre-Bulle, A. B. Stilgoe, H. Rubinsztein-Dunlop, *et al.*, "Optical trapping of otoliths drives vestibular behaviours in larval zebrafish," Nat. Commun. **8**, 630 (2017).

40. X. Zhang, B. Gu, and C. W. Qiu, "Force measurement goes to femto-Newton sensitivity of single microscopic particle," Light Sci. Appl. **10**, 243 (2021).

41. I. D. Stoev, B. Seelbinder, E. Erben, *et al.*, "Highly sensitive force measurements in an optically generated, harmonic hydrodynamic trap," eLight **1**, 7 (2021).

42. T. Pan, Y. Shi, N. Zhao, *et al.*, "Bio-micromotor tweezers for noninvasive bio-cargo delivery and precise therapy," Adv. Funct. Mater. **32**, 2111038 (2022).

43. M. E. J. Friese, T. A. Nieminen, N. R. Heckenberg, *et al.*, "Optical alignment and spinning of laser-trapped microscopic particles," Nature **394**, 348–350 (1998).

44. H. Crichton and P. Marston, "The measurable distinction between the spin and orbital angular momenta of electromagnetic radiation," Electron. J. Differ. Eq. **4**, 37–50 (2000).

45. S. S. Kruk, Z. J. Wong, E. Pshenay-Severin, *et al.*, "Magnetic hyperbolic optical metamaterials," Nat. Commun. **7**, 11329 (2016).

46. S. Lang, H. Lee, A. Y. Petrov, *et al.*, "Gold-silicon metamaterial with hyperbolic transition in near infrared," Appl. Phys. Lett. **103**, 021905 (2013).

47. P. Kelly, M. Liu, and L. Kuznetsova, "Designing optical metamaterial with hyperbolic dispersion based on an Al:ZnO/ZnO nano-layered structure using the atomic layer deposition technique," Appl. Opt. **55**, 2993–2997 (2016).

48. F. M. White, *Fluid Mechanics* (The McGraw Hill, 2008).